STING-driven interferon signaling triggers metabolic alterations in pancreas cancer cells visualized by [^{18}F]FLT PET imaging

Keke Liang[a,b,1], Evan R. Abt[c,d,1], Thuc M. Le[c,d], Arthur Cho[e], Amanda M. Dann[a,f], Jing Cui[g], Luyi Li[a], Khalid Rashid[c,d], Amanda L. Creech[c,d], Liu Wei[c,d], Razmik Ghukasyan[a,f], Ethan W. Rosser[c,d], Nanping Wu[a], Giuseppe Carlucci[c,d], Johannes Czernin[c,d,h], Timothy R. Donahue[a,c,d,f,h,2], and Caius G. Radu[c,d,h,2]

[a]Department of Surgery, University of California, Los Angeles, CA 90095; [b]Department of General Surgery/Pancreatic and Thyroid Surgery, Shengjing Hospital of China Medical University, Shenyang 110004, China; [c]Department of Molecular and Medical Pharmacology, University of California, Los Angeles, CA 90095; [d]Ahmanson Translational Theranostics Division, University of California, Los Angeles, CA 90095; [e]Department of Nuclear Medicine, Yonsei University College of Medicine, Seoul 03722, South Korea; [f]David Geffen School of Medicine, University of California, Los Angeles, CA 90095; [g]Department of Pancreatic Surgery, Union Hospital, Tongji Medical College, Huazhong University of Science and Technology, Hubei 430022, China; and [h]Jonsson Comprehensive Cancer Center, University of California, Los Angeles, CA 90095

Edited by Michael Karin, University of California San Diego, La Jolla, CA, and approved July 26, 2021 (received for review March 19, 2021)

Type I interferons (IFNs) are critical effectors of emerging cancer immunotherapies designed to activate pattern recognition receptors (PRRs). A challenge in the clinical translation of these agents is the lack of noninvasive pharmacodynamic biomarkers that indicate increased intratumoral IFN signaling following PRR activation. Positron emission tomography (PET) imaging enables the visualization of tissue metabolic activity, but whether IFN signaling–induced alterations in tumor cell metabolism can be detected using PET has not been investigated. We found that IFN signaling augments pancreatic ductal adenocarcinoma (PDAC) cell nucleotide metabolism via transcriptional induction of metabolism-associated genes including thymidine phosphorylase (TYMP). TYMP catalyzes the first step in the catabolism of thymidine, which competitively inhibits intratumoral accumulation of the nucleoside analog PET probe 3′-deoxy-3′-[^{18}F]fluorothymidine ([^{18}F]FLT). Accordingly, IFN treatment up-regulates cancer cell [^{18}F]FLT uptake in the presence of thymidine, and this effect is dependent upon TYMP expression. In vivo, genetic activation of stimulator of interferon genes (STING), a PRR highly expressed in PDAC, enhances the [^{18}F]FLT avidity of xenograft tumors. Additionally, small molecule STING agonists trigger IFN signaling–dependent TYMP expression in PDAC cells and increase tumor [^{18}F]FLT uptake in vivo following systemic treatment. These findings indicate that [^{18}F]FLT accumulation in tumors is sensitive to IFN signaling and that [^{18}F]FLT PET may serve as a pharmacodynamic biomarker for STING agonist–based therapies in PDAC and possibly other malignancies characterized by elevated STING expression.

interferon | STING | PET imaging | nucleotide metabolism | pancreatic cancer

Type I interferons (IFNs) are pleiotropic cytokines that are well studied for their multifaceted roles in stimulating anticancer and antiviral immune responses (1). While recombinant type I IFNs (IFN-α2a and IFN-α2b) have been evaluated as antitumor agents, vaccine adjuvants, and antiviral therapies, they are associated with pharmacokinetic limitations (2, 3). An emerging approach to overcome this obstacle involves the stimulation of endogenous IFN production using synthetic small molecule agonists of pattern recognition receptors (PRRs), which govern endogenous production of IFNs. PRR-regulated signaling pathways are stimulated by pathogen-associated factors, such as RNA degradation products, or alternatively by mislocalized self nucleic acids (4, 5). PRRs initiate a multifaceted cytokine response that moderates a diverse but coordinated set of anticancer and antipathogen effects (6). The recent development and translation of PRR pathway activators, including agonists of toll-like receptors and stimulator of interferon genes (STING), has reinvigorated the investigation of therapeutic IFN amplification in the context of cancer immunotherapy (7).

STING, a key regulator of IFN production, has emerged as a promising immunotherapeutic target in cancer (8). Several iterations of STING agonists have been investigated in preclinical and clinical settings and have been shown to stimulate antitumor CD8$^+$ T cell responses that are potentiated by cytotoxic therapy or immune checkpoint blockade combinations (NCT03172936, NCT02675439, and NCT03843359) (9–11). While initial approaches to target STING centered on analogs of the endogenous STING ligand 2′-3′-cyclic guanosine monophosphate–adenosine monophosphate (cGAMP) and required intratumoral administration, synthetic STING agonists with systemic activity have recently been described and are under clinical investigation (NCT03843359) (7, 10). It is thought that IFN signaling triggered by STING agonists will be particularly beneficial in the context of immunologically cold, T cell–excluded tumors such as pancreatic ductal adenocarcinoma (PDAC). Importantly, PDAC is characterized by high expression of STING, which is detectable in the cancer cell

Significance

Our findings indicate that interferon signaling induces metabolic alterations in pancreas cancer cells which can be visualized in vivo by noninvasive 3′-deoxy-3′-[^{18}F]fluorothymidine positron emission tomography (PET) imaging. Therefore, PET imaging may have utility as a pharmacodynamic readout in the translation of emerging interferon-inducing therapies, including STING agonists, for cancer therapy.

Author contributions: K.L., E.R.A., T.R.D., and C.G.R. designed research; K.L., E.R.A., T.M.L., A.C., A.M.D., J. Cui, L.L., K.R., A.L.C., L.W., R.G., E.W.R., and N.W. performed research; G.C. and J. Czernin contributed new reagents/analytic tools; K.L. and E.R.A. analyzed data; T.M.L. performed mass spectrometry analysis; A.C. and L.W. performed PET imaging studies and analyzed PET imaging data; L.L. generated cell line models; G.C. provided PET tracers; and E.R.A. and C.G.R. wrote the paper.

Competing interest statement: C.G.R. and J. Czernin are cofounders of Sofie Biosciences and the Trethera Corporation. They and the University of California hold equity in Sofie Biosciences and the Trethera Corporation. T.R.D. is an executive board member and holds equity in the Trethera Corporation.

This article is a PNAS Direct Submission.

See online for related content such as Commentaries.

[1]K.L. and E.R.A. contributed equally to this work.

[2]To whom correspondence may be addressed. Email: cradu@mednet.ucla.edu or tdonahue@mednet.ucla.edu.

This article contains supporting information online at https://www.pnas.org/lookup/suppl/doi:10.1073/pnas.2105390118/-/DCSupplemental.

Published September 3, 2021.

compartment of tumors (12). Additionally, PDAC cells are capable of sensing and responding to alterations in local IFN levels, and tumor cell–intrinsic IFN responses contribute to the efficacy of STING agonists in PDAC models (13).

A challenge in the translation of STING agonists is the identification of pharmacodynamic biomarkers to track the localization and duration of downstream IFN-driven responses. Mechanistically, IFNs function by binding a dimeric receptor comprised of IFNAR1/IFNAR2, which initiates a Janus kinase1 (JAK1)/TYK2-mediated signaling cascade that stimulates ISGF3 transcription factor complex activation and, ultimately, the transcriptional up-regulation of interferon-stimulated genes (ISGs) (2). Effector ISGs have diverse biological functions but operate together to initiate and sustain antipathogen responses. Importantly, ISG expression is temporally uncoupled from the binding of IFNs to their receptors, and ISG expression driven by unphosphorylated

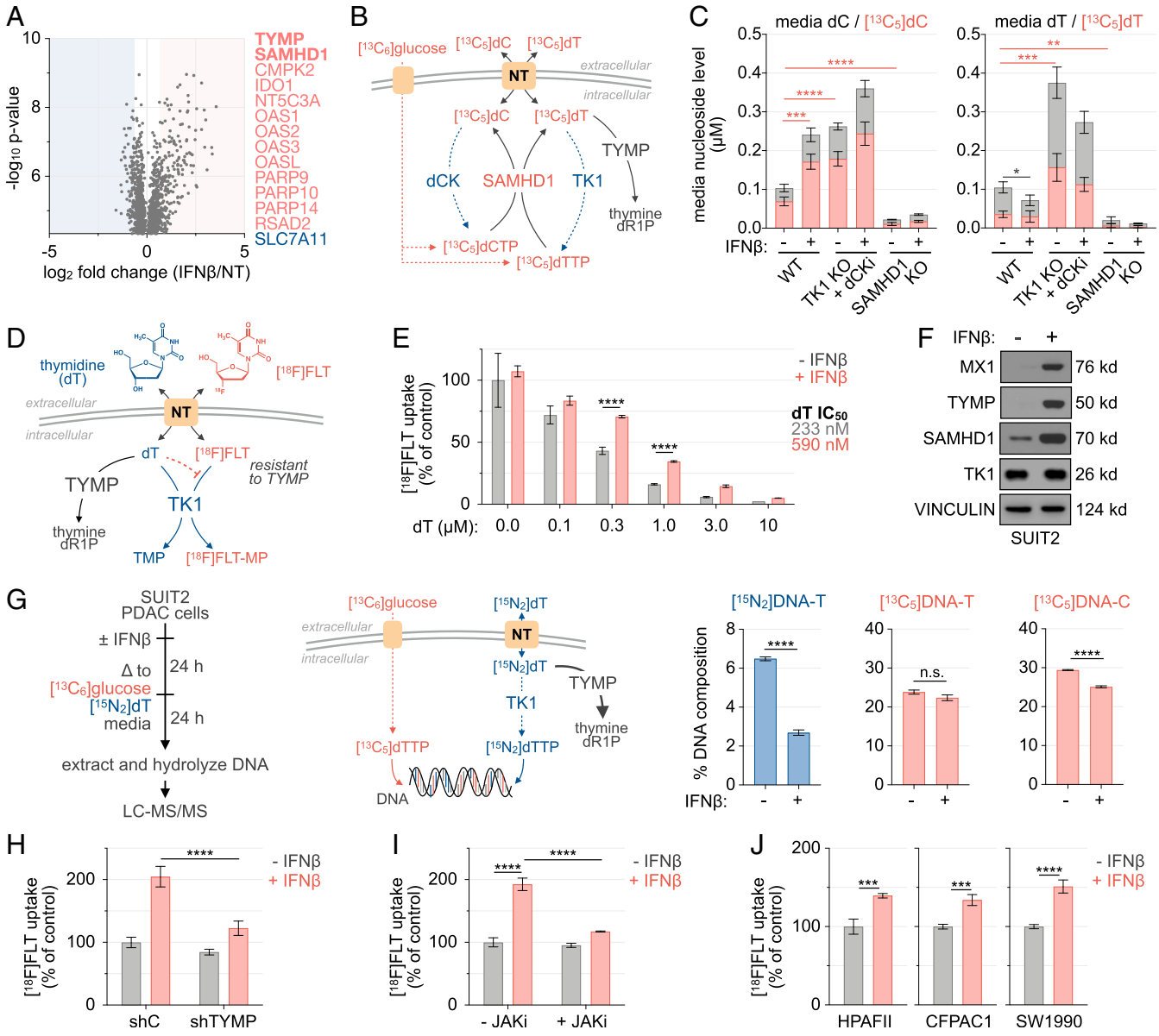

Fig. 1. Type I IFN signaling promotes TYMP-dependent [^{18}F]FLT uptake in PDAC cells. (*A*) RNA-seq analysis of SUIT2 cells treated ± 100 U/mL IFN-β for 24 h ($n = 3$; FDR < 0.01%). (*B*) Schematic of the regulation of dT and dC levels by SAMHD1, TYMP, dCK, and TK1. NT: nucleoside transporter. (*C*) LC-MS/MS analysis of media dC and dT levels from SUIT2 parental, TK1 CRISPR/Cas9 KO, and SAMHD1 KO cell cultures treated ± 100 U/mL IFN-β for 24 h supplemented with 1 g/L [$^{13}C_6$]glucose. TK1 KO cells were treated + 1 μM DI-82 (dC*Ki*; mean ± SD; $n = 3$; one-way ANOVA corrected for multiple comparisons by Bonferroni adjustment). Unlabeled and [$^{13}C_6$]glucose-labeled media nucleoside fractions are indicated. (*D*) Regulation of [^{18}F]FLT accumulation by competition with dT. (*E*) [^{18}F]FLT uptake in SUIT2 cells treated ± 100 U/mL IFN-β for 24 h and subsequently pulsed with 5 μCi [^{18}F]FLT alongside indicated concentrations of dT for 2 h (mean ± SD; $n = 3$; unpaired *t* test). Insert indicates half maximal inhibitory concentration (IC_{50}) of dT for inhibition of [^{18}F]FLT uptake. (*F*) Immunoblot analysis of SUIT2 cells treated ± 100 U/mL IFN-β for 24 h. (*G*) Incorporation of [$^{13}C_6$]glucose and [$^{15}N_2$]dT into newly replicated thymidine in DNA (DNA-T) and deoxycytidine in DNA (DNA-C) evaluated using LC-MS/MS. SUIT2 cells were treated ± 100 U/mL IFN-β for 24 h and transitioned to media containing 1 g/L [$^{13}C_6$]glucose + 1 μM [$^{15}N_2$]dT ± IFN-β for 24 h. (mean ± SD; $n = 3$; unpaired *t* test). (*H*) [^{18}F]FLT uptake in SUIT2 shControl (shC) and shTYMP cells treated ± 100 U/mL IFN-β for 24 h performed as in *E* (mean ± SD; $n = 3$; one-way ANOVA corrected for multiple comparisons by Bonferroni adjustment). (*I*) [^{18}F]FLT uptake in SUIT2 cells treated ± 100 U/mL IFN-β ± 1 μM ruxolitinib (JAK*i*) for 24 h performed as in *E* (mean ± SD; $n = 3$; one-way ANOVA corrected for multiple comparisons by Bonferroni adjustment). (*J*) [^{18}F]FLT uptake in HPAFII, CFPAC1, and SW1990 cells performed as in *E* (mean ± SD; $n = 3$; unpaired *t* test). *$P < 0.05$; **$P < 0.01$; ***$P < 0.001$; ****$P < 0.0001$.

STAT-containing ISGF3 complexes can persist in the absence of IFN following an initial signal (14). Thus, neither the measurement of PRR agonist or IFN levels is sufficient to infer IFN signaling responses and ISG expression. Therefore, we aimed to identify noninvasive approaches suitable for the tracking of ISG expression downstream of STING activation in vivo.

Positron emission tomography (PET) is a highly adaptable, noninvasive diagnostic technology that enables detection and quantification of radionuclide-labeled probe biodistribution in vivo. PET has proven to be particularly well suited for the visualization of biochemical pathway activity through the tracking of metabolite probes, which include [^{18}F]-labeled analogs of glucose, amino acids, and nucleosides (15–18). While multiple factors contribute to metabolite analog PET probe accumulation in tissues, new insight into the determinants influencing their uptake can enable the repurposing of these probes as biomarkers for emerging therapies. Recently, IFNs have been linked to metabolic reprogramming in tumor cells through the transcriptional regulation of metabolism-linked ISGs (19). However, whether these metabolic effects of IFNs can be visualized by noninvasive imaging approaches, such as PET, has not been investigated. We reasoned that a systematic evaluation of IFN-induced metabolic reprogramming and the identification of metabolic pathways linked to the uptake of metabolite analog PET probes could enable the development and translation of noninvasive imaging strategies to track STING agonist-driven IFN signaling in vivo.

Results

Type I IFN Induces Thymidine Phosphorylase–Dependent 3′-deoxy-3′-[^{18}F]fluorothymidine Accumulation in PDAC Cells. Aiming to identify metabolic networks transcriptionally altered by IFN exposure, we performed RNA-sequencing (RNA-seq) analysis of SUIT2 PDAC cells treated with or without type I IFN (IFN-β) for 24 h. In addition to canonical ISGs, we detected alterations (>2 fold-change, false discovery rate [FDR] < 0.01%) in the expression of metabolism-related genes associated with various metabolic pathways (Fig. 1*A*). IFN altered the expression of genes associated with tryptophan metabolism (IDO1) and NAD^+/NADH metabolism (PARP9/10/14), consistent with previous findings from our group (19). IFN triggered transcriptional down-regulation of the cysteine–glutamate antiporter (SLC7A11), which has been shown to be down-regulated in tumor cells following exposure to type II IFN in combination with ionizing radiation (20). We also observed up-regulation of genes associated with nucleoside production (sterile alpha motif and HD domain–containing protein 1 [SAMHD1]) and breakdown (thymidine phosphorylase [TYMP]). Importantly, nucleoside levels have been shown to critically determine the uptake of nucleoside analog PET probes such as 3′-deoxy-3′-[^{18}F]fluorothymidine (FLT) and 2-chloro-2'-deoxy-2'-[^{18}F]fluoro-9-β-d-arabinofuranosyl-adenine (CFA) (21, 22). Taken together, these observations suggested that IFN signaling could influence nucleoside analog PET probe accumulation in tumor cells via the modulation of nucleoside levels.

Via deoxyribonucleotide triphosphate (dNTP) phosphohydrolysis, the ISG SAMHD1 mediates the production of various deoxyribonucleosides (dNs), which each have unique metabolic fates (23). While purine dNs are rapidly degraded, deoxycytidine (dC) produced via deoxycytidine triphosphate (dCTP) phosphohydrolysis can be either recaptured by cells via deoxycytidine kinase (dCK), effluxed into the environment via equilibrative nucleoside transporters (ENT), or broken down by cytidine deaminase (CDA). In parallel, SAMHD1-produced thymidine (dT) is either phosphorylated and trapped by thymidine kinase 1 (TK1), released via ENT, or catabolized by TYMP, which liberates the thymine nucleobase from the deoxyribose sugar (Fig. 1*B*). To investigate the impact of IFN and the roles of nucleoside kinases on dN efflux in PDAC cells, we generated SUIT2 SAMHD1 knockout (KO) cells, SUIT2 TK1 KO cells (*SI Appendix*, Fig. S1 *A* and *B*), and additionally utilized a small molecule dCK inhibitor (DI-82) developed by our group (24). We employed liquid chromatography mass spectrometry (LC-MS/MS) in the multiple reaction monitoring (MRM) mode to evaluate media nucleoside levels following treatment in the presence of [$^{13}C_6$]glucose, which enables the tracking of newly synthesized metabolites (25). We found that IFN treatment enhances SAMHD1-dependent efflux of glucose-labeled dC ([$^{13}C_5$]dC), which is further potentiated by dCK inhibition (Fig. 1*C*). In contrast, while TK1 KO enhanced and SAMHD1 KO diminished dT efflux, dT levels decreased following IFN treatment, suggesting that IFN-induced TYMP reduces environmental dT (Fig. 1*C*).

Given that both intrinsically high TYMP expression and exogenous administration of TYMP have been shown to promote tumor FLT PET probe accumulation in vivo through the depletion of native dT (21, 26), we reasoned that TYMP induction by IFN could be leveraged for the detection of IFN signaling responses using PET imaging. [^{18}F]FLT is an analog of dT and a substrate for the cell cycle S-phase restricted/TK1-mediated pyrimidine salvage pathway, which functions in parallel with the de novo pathway to synthesize deoxythymidine triphosphate (dTTP) for DNA replication and repair (18, 27). Mechanistically, TYMP drives [^{18}F]FLT uptake in tumors by catalyzing the breakdown of dT, which competes with [^{18}F]FLT for phosphorylation and intracellular trapping by TK1 (Fig. 1*D*) (18, 28). Additionally, the fluorine substitution renders FLT resistant to TYMP-mediated degradation and significantly decreases its affinity for TK1 (26). Thus, [^{18}F]FLT accumulation in tissues is a marker for both the degree of TK1 expression (a function of proliferation) and local dT abundance, which is regulated by TYMP. To determine the impact of IFN signaling on [^{18}F]FLT uptake, we cultured SUIT2 cells in the presence of IFN-β for 24 h and subsequently pulsed cells with [^{18}F]FLT alongside varying concentrations of dT. While IFN-β did not alter [^{18}F]FLT uptake in the absence of dT, probe uptake in the presence of 1 μM dT was increased >twofold by IFN-β pretreatment (Fig. 1*E*). This result indicated that decreased competition between [^{18}F]FLT and dT, and not alterations in the expression or activity of TK1, likely underlies IFN-β–induced increases in probe uptake. Consistently, IFN treatment elevated the protein levels of MX1, TYMP, and SAMHD1 but had no effect on TK1 (Fig. 1*F*).

To obtain further evidence in support of this model, we utilized a dual stable isotope-labeled metabolite tracking approach coupled with LC-MS/MS-MRM to evaluate the impact of IFN signaling on the discrete contributions of de novo and salvage pathways DNA replication, in particular to dT in newly replicated DNA (DNA-T) (29). For this experiment, 24 h after treatment ± IFN-β, SUIT2 cells were transitioned to media containing [$^{13}C_6$]glucose (to track de novo pathway activity) and [$^{15}N_2$]dT (to track salvage pathway activity) for an additional 24 h before DNA purification (Fig. 1*G*). Isolated DNA was hydrolyzed to release nucleosides, which were analyzed by LC-MS/MS-MRM. IFN signaling selectively impaired the ability of [$^{15}N_2$]dT to contribute to DNA-T, while it did not significantly alter the contribution of [$^{13}C_6$]glucose newly synthesized DNA-T. In summary, IFN signaling enhances [^{18}F]FLT uptake in PDAC cells in the presence of dT while restricting the ability of cells to utilize extracellular dT for DNA replication.

To confirm a role for TYMP as an IFN-regulated mediator of [^{18}F]FLT uptake, we knocked down TYMP in SUIT2 cells using short hairpin RNA (shRNA) and found that the IFN-β–induced increase in [^{18}F]FLT probe accumulation was lost upon TYMP silencing (Fig. 1*H* and *SI Appendix*, Fig. S1*C*). Additionally, Janus kinase 1/2 (JAK1/2) inhibition using ruxolitinib prevented IFN-β–induced [^{18}F]FLT uptake (Fig. 1*I*), while type II IFN (IFN-γ) promoted [^{18}F]FLT accumulation in SUIT2 cells (*SI Appendix*, Fig. S1*D*). To expand our findings, we performed immunoblot analysis of a panel of PDAC cell lines treated with

IFN-β and found that all models are capable of recognizing and responding to type I IFN, as evidenced by MX1 induction, and that TYMP is an ISG in the majority (20/21) of models (*SI Appendix*, Fig. S1 *E* and *F*). Furthermore, IFN-β–induced potentiation of [^{18}F]FLT uptake in the presence of dT was observed in HPAFII, CFPAC1, and SW1990 PDAC cells (Fig. 1*J*). To investigate the lack of TYMP protein in PATU8988T cells, and given that TYMP is epigenetically suppressed in a subset of cancers, we interrogated TYMP expression and promoter methylation across cell lines annotated in the DepMap genomics repository (30, 31). PATU8988T not only possess the lowest TYMP expression among PDAC cell lines but also exhibited a uniquely high degree of TYMP promoter methylation (*SI Appendix*, Fig. S1*G*). Consistently, treatment with the DNA methyltransferase inhibitor decitabine in the presence of IFN-β unlocked TYMP expression (*SI Appendix*, Fig. S1 *H* and *I*). As PDAC tumors characteristically contain a significant stromal cell compartment, we evaluated the effect of IFN-β on a human PDAC cancer-associated fibroblast (CAF) model and observed elevated TYMP protein levels (*SI Appendix*, Fig. S1*J*) (32). In summary, we determined that IFN promotes [^{18}F]FLT PET probe accumulation in PDAC cells in vitro through the transcriptional up-regulation of TYMP and the depletion of dT, an endogenous inhibitor of [^{18}F]FLT uptake.

IFN Signaling Initiated by STING Triggers TYMP Expression In Vitro and In Vivo. To build on our observation that recombinant IFN induces TYMP expression and [^{18}F]FLT uptake, we next asked if tumor cell–autonomous IFN signaling initiated downstream of PRR activation elicits comparable transcriptional and metabolic alterations. In contrast to most PRRs, which are predominantly expressed in immune cells, STING, the adaptor protein for the cyclic GMP-AMP synthase (cGAS)-mediated cytosolic DNA sensing pathway, is widely expressed in immune, stromal, endothelial, and epithelial cells as well as in subsets of tumor cells (33). While STING has been shown to have tumor suppressor–like functions and is thus silenced in specific cancers, particularly those associated with high mutational burden, STING is expressed in the tumor cell compartment of PDAC tumors (8, 12). Therefore, our subsequent studies focused on PDAC cell autonomous IFN-signaling initiated downstream of STING activation. STING is widely expressed across PDAC cell line models (*SI Appendix*, Fig. S1*K*), and STING functionality in SUIT2 cells was confirmed by demonstrating an up-regulation of the *IFNB1* transcript following transfection with a bisphosphorothioate 2′-3′-cGAMP analog (*SI Appendix*, Fig. S1*L*). We also observed that SUIT2 cells are cGAS deficient, as *IFNB1* transcript levels were unaltered by following transfection with interferon stimulatory DNA (ISD; *SI Appendix*, Fig. S1*L*).

To investigate the role of STING in regulating PDAC IFN signaling and tumor growth in vivo, SUIT2 were engineered to express a constitutively active STING mutant (SUIT2-TetR-STING^{R284M}) under the control of a doxycycline (DOX)-inducible promoter (Fig. 2*A*) (19, 34). This genetic system enabled an investigation of the consequences of tumor cell–autonomous STING activation on IFN signaling and metabolic alterations in vitro and in vivo. STING^{R284M} activation using DOX in vitro impaired PDAC cell proliferation in three-dimensional culture and triggered TYMP expression, which was prevented by JAK1/2 inhibition (Fig. 2 *B* and *C*). In parallel, we evaluated the growth and IFN signaling profile of SUIT2-TetR-STING^{R284M} subcutaneous xenograft tumors in mice treated with or without DOX. Activation of STING^{R284M} restricted SUIT2 tumor growth (Fig. 2*D*), and immunoblot analysis of resected tumors revealed that STING^{R284M} activation resulted in enhanced TYMP expression but had no consistent effect on TK1 protein levels (Fig. 2*E*). Consistently, LC-MS/MS analysis of tumor metabolite levels indicated that dT, but not dC, was decreased by STING activation (Fig. 2*F*). In xenograft tumors, ISG expression downstream of STING activation relies on tumor cell–initiated autocrine/paracrine IFN signaling, as type I IFNs are species restricted. Collectively, these results indicate that STING activation in PDAC cells triggers TYMP expression in vitro and in vivo.

STING-induced Metabolic Alterations Are Visualized by [^{18}F]FLT PET. To determine if genetic STING activation alters PET probe accumulation in tumors, we inoculated SUIT2-TetR-STING^{R284M} cells into either the flank or pancreas of immunodeficient mice, treated with or without DOX and evaluated [^{18}F]-labeled probe biodistribution using sequential PET/computed tomography (CT) imaging (Fig. 3*A*). We investigated alterations in [^{18}F]FLT uptake alongside 2'-deoxy-2'-[^{18}F]fluoro-D-glucose ([^{18}F]FDG; an analog of glucose) and 2'-deoxy-2'-[^{18}F]fluoro-β-D-arabinofuranosylcytosine ([^{18}F]FAC (ref. 15), an analog of deoxycytidine and a substrate for dCK) to comprehensively determine the impact of STING activation on metabolite analog PET probe accumulation in tumors.

In the subcutaneous model, we performed a serial assessment of intratumoral [^{18}F]FLT and [^{18}F]FDG PET probe accumulation on days 7 and 8, respectively, after DOX initiation (Fig. 3*A*). In this model, the [^{18}F]FLT signal was significantly increased following STING activation. This alteration was restricted to [^{18}F]FLT, as tumor [^{18}F]FDG accumulation in the same animal following serial imaging was unaffected by STING^{R284M} induction (Fig. 3*A*). Consistently, we did not observe alterations in the expression of glucose uptake mediators following IFN treatment in vitro (Fig. 1*A*). Increased [^{18}F]FLT uptake was also observed in orthotopic PDAC tumors after DOX administration (Fig. 3*B*). In an independent cohort of subcutaneous tumor-bearing mice, intratumoral [^{18}F]FAC accumulation was not responsive to genetic STING activation (*SI Appendix*, Fig. S2*A*). DOX treatment of tumor-bearing mice did not result in significant alterations in plasma dT levels, indicating that STING^{R284M}-mediated TYMP induction in tumors is insufficient to modulate nucleoside levels systemically (*SI Appendix*, Fig. S2*B*). Consistently, serial [^{18}F]FLT and [^{18}F]FDG imaging of DOX-treated mice bearing bilateral SUIT2-TetR-GFP, which conditionally express GFP, and SUIT2-TetR-STING^{R284M} tumors revealed that [^{18}F]FLT, and not [^{18}F]FDG accumulation, is selectively enhanced in STING^{R284M}-expressing tumors (*SI Appendix*, Fig. S2 *C* and *D*). This finding indicated that STING-induced alterations in dT metabolism are confined locally in tumors and that [^{18}F]FLT alterations are not an artifact of DOX treatment alone. We investigated this effect in an additional cohort of orthotopic tumor-bearing mice in which the number of SUIT2-TetR-STING^{R284M} cells inoculated was decreased from 30,000 to 5,000 cells and in which imaging was performed at an earlier timepoint (*SI Appendix*, Fig. S2*E*). We confirmed that genetic STING activation increases tumor [^{18}F]FLT uptake in this experimental setting (*SI Appendix*, Fig. S2 *F* and *G*). Furthermore, as STING^{R284M}-active tumors exhibited restricted growth, our results add to the growing body of evidence demonstrating that [^{18}F]FLT accumulation is not solely a marker of tumor cell proliferation rate but is instead a function of both TK1 expression/activity and environmental dT levels (21, 35). Taken together, these findings confirm that genetic STING activation selectively and potently enhances the avidity of PDAC tumors toward [^{18}F]FLT.

STING Activation by Small Molecule Agonists Drives TYMP Expression and Promotes [^{18}F]FLT Accumulation In Vitro and In Vivo. Pharmacological STING activation, enabled by the development of systemically bioavailable STING agonists, which are currently under clinical evaluation for the treatment of solid tumors, is a promising immunotherapeutic approach to enhance antitumor adaptive immune responses (NCT03843359) (7). However, the impact of small molecule synthetic STING agonists on autocrine

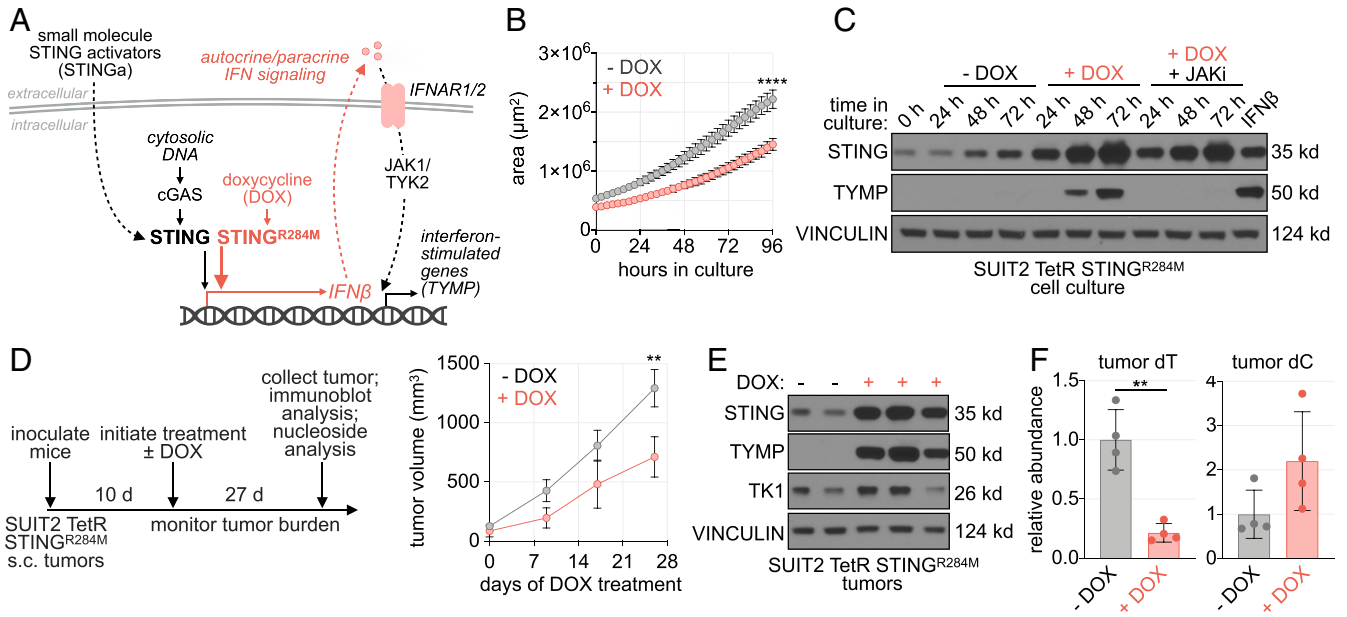

Fig. 2. STING activation up-regulates TYMP expression in vitro and in vivo. (*A*) Schematic of autocrine/paracrine IFN signaling regulation by the cGAS/STING pathway. (*B*) Live-cell imaging analysis of SUIT2-TetR-STING^{R284M} cells treated ± 50 ng/mL DOX in anchorage-independent culture (mean ± SD; $n = 6$; unpaired *t* test). (*C*) Immunoblot analysis of SUIT2-TetR-STING^{R284M} cells treated ± 50 ng/mL DOX ± 1 μM ruxolitinib (JAKi) as indicated or 100 U/mL IFN-β for 24 h. (*D*) Growth of SUIT2-TetR-STING^{R284M} subcutaneous (s.c.) xenograft tumors in mice treated ± DOX. Tumor volumes were monitored by CT (mean ± SD; $n = 8$; unpaired *t* test). (*E*) Immunoblot analysis of individual tumors from the end point of the experiment in *D*. (*F*) LC-MS/MS analysis of dT and dC levels in SUIT2-TetR-STING^{R284M} tumors from mice treated ± DOX (mean ± SD; $n = 4$, unpaired *t* test). $^{**}P < 0.01$; $^{****}P < 0.0001$.

IFN signaling and ISG expression in PDAC cells has not been investigated.

The synthetic STING agonist diABZI-compound 3 (STINGa) triggered a dose-dependent increase of *IFNB1* and *TYMP* transcripts in SUIT2 cells (Fig. 4*A* and *SI Appendix*, Fig. S3*A*) (7). Then, 4 h after STINGa treatment, SUIT2 cells exhibited multiple markers of cGAS/STING pathway activation, including IRF3-S386 phosphorylation, STING-S366 phosphorylation, and a decrease in STING protein levels (*SI Appendix*, Fig. S3*B*) (36). After this, 24 h of STINGa treatment was required to observe an increase in TYMP protein levels (*SI Appendix*, Fig. S3*B*). Signaling through JAK1/2 was dispensable for STINGa-induced IRF3-S386 phosphorylation but essential for the induction of TYMP (*SI Appendix*, Fig. S3*C*). Consistently, KO of IFNAR1 in SUIT2 cells prevented STINGa-mediated TYMP and STAT1 induction but had no effect on IRF3-S386 phosphorylation (Fig. 4*B*). Metabolically, STINGa treatment enhanced [^{18}F]FLT uptake in SUIT2 cells in the presence of dT, and this alteration was dependent on IFNAR1 expression (Fig. 4*C*). STINGa treatment up-regulated TYMP protein levels in a panel of STING-proficient PDAC cell lines and significantly enhanced the uptake of [^{18}F]FLT in CFPAC1 cells (*SI Appendix*, Fig. S3 *D* and *E*). These findings indicate that STINGa treatment enhances TYMP expression and activity downstream of autocrine/paracrine IFN signaling in PDAC cells.

To determine whether STINGa activates IFN signaling responses and triggers ISG expression in PDAC xenograft tumors in vivo, we employed two orthogonal approaches. First, we employed SUIT2 cells that were engineered to stably express a firefly luciferase (fLUC)-linked IFN-stimulated response element (ISRE) reporter, which enables the noninvasive tracking of IFN signaling in vivo using bioluminescence (BLI) imaging (37). Mice bearing subcutaneous SUIT2 ISRE-fLUC tumors were treated with a single intravenous dose of STINGa, and the tumor BLI signal was monitored longitudinally following treatment (Fig. 4*D*). ISRE reporter activity was induced as early as 3 h after STINGa administration and remained elevated up to 48 h after treatment. Additionally, we collected subcutaneous SUIT2 tumors after STINGa treatment and performed an immunoblot analysis of STING and IFN signaling. STINGa treatment effectively activated the cGAS/STING pathway in tumors and elicited autocrine/paracrine IFN signaling 4 h after treatment as evidenced by elevations in STING-S366, IRF3-S386, and STAT1-Y701 phosphorylation. In contrast, induction of the ISGs TYMP, MX1, and STAT1 was only apparent 24 h after treatment (Fig. 4*E*). This analysis indicates a marked temporal discordance between cGAS/STING activity, IFN production, and ISG expression in tumor cells elicited by systemic STINGa treatment. Together, our in vitro and in vivo observations indicate that small molecule synthetic STING agonists trigger autocrine/paracrine IFN signaling and ISG expression in PDAC cells.

Given that genetic STING activation in xenograft tumors increased [^{18}F]FLT accumulation, we next determined if systemic STINGa treatment elicits similar effects. Mice bearing subcutaneous SUIT2 tumors were treated with two intravenous doses of STINGa and evaluated using [^{18}F]FLT PET/CT analysis 72 h after the second treatment (Fig. 5*A*). STING agonist treatment significantly increased the [^{18}F]FLT avidity of SUIT2 subcutaneous tumors (Fig. 5*A*). Immunoblot analysis of tumors resected immediately after PET/CT analysis confirmed that STINGa treatment promoted the expression of TYMP and MX1 while not impacting the levels of TK1 (*SI Appendix*, Fig. S4*A*). To evaluate the generalizability of this observation, we performed [^{18}F]FLT PET/CT analysis of mice bearing subcutaneous CFPAC1 xenograft tumors following STINGa treatment (*SI Appendix*, Fig. S4*B*). In CFPAC1 tumors, we observed a trend of STINGa-induced elevation in intratumoral [^{18}F]FLT accumulation and enhanced expression of TYMP despite this model exhibiting high basal expression of ISGs such as MX1 (*SI Appendix*, Fig. S4 *C* and *D*). Systemic STING agonist treatment also enhanced the [^{18}F]FLT avidity of orthotopic SUIT2 tumors (Fig. 5*B*). Collectively, these results demonstrate that intratumoral [^{18}F]FLT PET probe accumulation is responsive to STING agonist treatment and

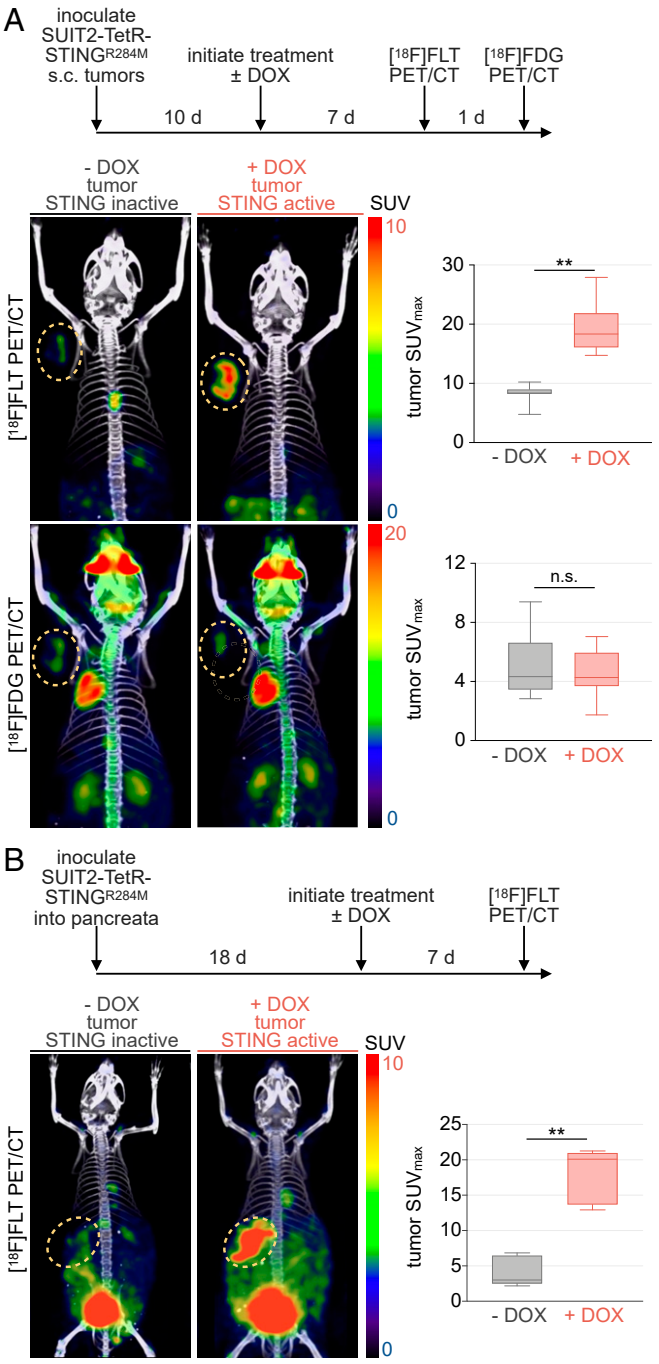

Fig. 3. STING signaling enhances PDAC tumor [^{18}F]FLT avidity. (*A*) [^{18}F]FLT and [^{18}F]FDG PET/CT imaging of mice bearing subcutaneous (s.c.) SUIT2--TetR-STING^{R284M} tumors following treatment ± DOX. Highlighted region indicates tumor (n = 4 to 5, two-tailed Mann–Whitney U test). (*B*) [^{18}F]FLT PET/CT imaging of mice bearing orthotopic SUIT2-TetR-STING^{R284M} tumors following treatment ± DOX (30,000 cells injected; n = 5, two-tailed Mann–Whitney U test). $^{**}P < 0.01$.

indicate that [^{18}F]FLT PET imaging could serve as an in vivo pharmacodynamic biomarker for IFN-inducing therapies.

Discussion

In this study, we have shown that [^{18}F]FLT PET visualizes TYMP-mediated alterations in the metabolism of dT downstream of IFN signaling and STING activation. Thus, this tracer may have utility as a pharmacodynamic biomarker for PRR agonists to track the duration and localization of IFN signaling responses which are not readily revealed through the evaluation of drug pharmacokinetics or serum cytokine levels.

The development of PET probes suitable for the visualization of proliferation has been a longstanding goal. Given that S-phase restricted TK1 is essential for the intracellular trapping of dT, radionuclide-labeled dT analogs, including [^{11}C]dT and [^{18}F]FLT, emerged as candidate tracers to monitor the proliferative capacity of tumor cells and response to treatment (18, 38–40). Clinically, [^{18}F]FLT uptake has been shown to positively correlate with Ki67 status in glioma (41), and additional studies indicate that chemotherapy-induced down-regulation of tumor [^{18}F]FLT signals may associate with tumor cell proliferation inhibition and therapy response (42–44). However, decades of preclinical and clinical research have provided substantial evidence that additional factors govern [^{18}F]FLT uptake. The relative activities of tumor cell de novo and salvage pathways for dTTP synthesis can influence probe accumulation as evidenced by studies demonstrating that the tumor [^{18}F]FLT signal increases acutely following de novo inhibition by thymidylate synthase (TYMS) inhibitors pemetrexed and TAS-120, which likely reflects a metabolic shift toward salvage (45, 46). A similar phenomenon was revealed by [^{11}C]dT PET in gastrointestinal cancer patients following TYMS inhibitor treatment (47). Beyond dTTP biosynthetic preference, native dT levels, which in turn are regulated by TYMP, SAMHD1 and TK1 critically influence probe trapping (21). Finally, probe metabolism, which varies across species, and dephosphorylation of [^{18}F]FLT nucleotides, which can occur during extended uptake periods, require consideration when defining uptake duration in preclinical and clinical studies (18, 48).

Nevertheless, we agree with previous conclusions that the variables associated with [^{18}F]FLT accumulation are potentially less relevant in the context of longitudinal studies in which baseline and posttreatment scans following intervention are obtained in individual patients (35). [^{18}F]FLT, along with other nucleoside-based PET probes, provides unique insight into the metabolic status of tissues in vivo, and a more complete understanding of the factors influencing their uptake can inform additional clinical contexts in which they can be effectively utilized, potentially as pharmacodynamic biomarkers for emerging therapies.

Emerging evidence has indicated that [^{18}F]FLT biodistribution in humans is responsive to immunotherapy. Elevated [^{18}F]FLT accumulation was observed in the spleen following anti-CTLA4 immunotherapy in melanoma patients (49), and [^{18}F]FLT PET has been applied to track antigen specific immune responses and stimulation of lymphocyte proliferation triggered by dendritic cell vaccination (50). The molecular mechanisms underlying these alterations are not fully understood, and the contribution of IFN signaling has not been explored. Together, these reports indicate that cellular metabolism is responsive to immunotherapeutic intervention and provide the rationale for further mechanistic investigations of the intersections between cytokine signaling, immune activation, and metabolic reprogramming.

The metabolic effects of IFNs are increasingly well appreciated, but their implications in tumor growth, metastasis, or therapy response is unclear (19, 51, 52). We have previously shown that IFNs trigger depletion of NAD^+/NADH pools in PDAC cells via the up-regulation of noncanonical PARPs and increase their reliance on NAM recycling through NAMPT (19). Beyond NAD^+/NADH metabolism, IFN-induced metabolic alterations may elicit additional actionable vulnerabilities that can be exploited using rationally designed combination therapies. In particular, capecitabine, an orally bioavailable prodrug of 5-fluorouracil (5-FU), may exhibit synergy with IFNs signaling, as TYMP expression is positively correlated with capecitabine efficacy in breast cancer patient-derived xenograft (PDX) models (53). The mechanism underlying TYMP-mediated capecitabine sensitization is likely multifactorial and may be a function of both of the following: 1) increased

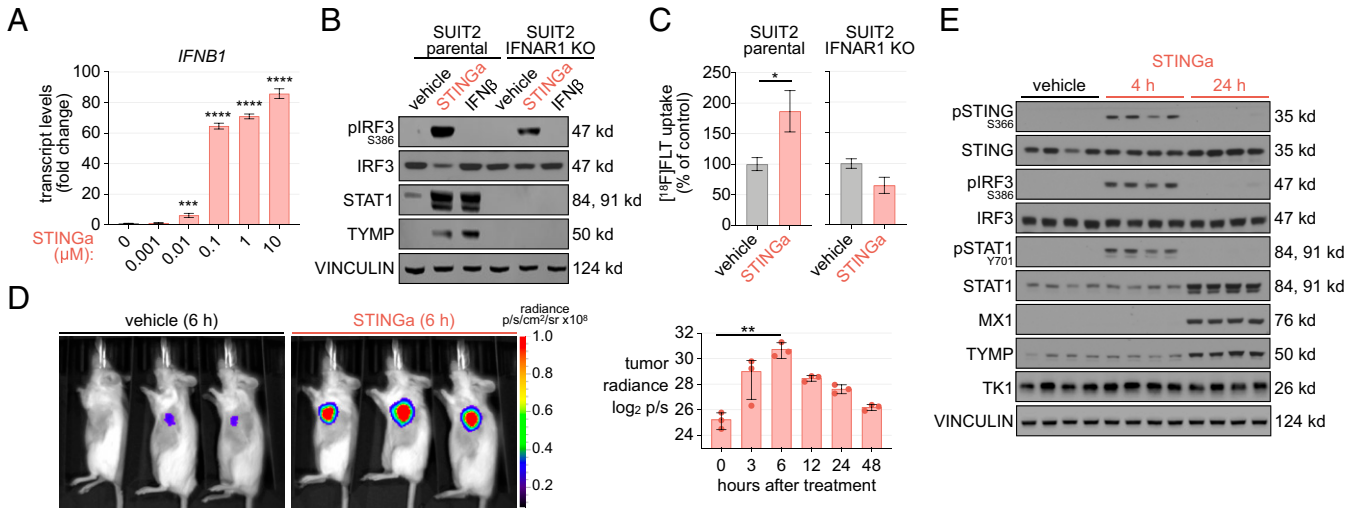

Fig. 4. Pharmacological STING activation up-regulates TYMP via autocrine type I IFN signaling. (*A*) RT-PCR analysis of *IFNB1* transcript levels in SUIT2 cells treated ± indicated doses of STINGa for 4 h (mean ± SD; $n = 3$; one-way ANOVA corrected for multiple comparisons by Bonferroni adjustment, all comparisons were made to vehicle control). (*B*) Immunoblot analysis of SUIT2 parental and IFNAR1 CRISPR/Cas9 KO cells treated ± 100 nM STINGa or 100 U/mL IFN-β for 24 h. (*C*) [^{18}F]FLT uptake in SUIT2 parental and IFNAR1 KO cells treated ± 1 μM STINGa for 72 h and subsequently pulsed with 5 μCi [^{18}F]FLT alongside 300 nM dT for 2 h (mean ± SD; $n = 3$; unpaired *t* test). (*D*) Bioluminescence imaging of NSG mice bearing subcutaneous (s.c.) SUIT2 ISRE-fluc tumors treated ± 1.5 mg/kg STINGa by intravenous (i.v.) injection ($n = 3$; mean ± SD; Kruskal–Wallis test corrected using Dunn's multiple comparisons test). (*E*) Immunoblot analysis of s.c. SUIT2 tumors isolated from NCG mice at the indicated time points following treatment with 1.5 mg/kg STINGa i.v. ($n = 4$/group). $^*P < 0.05$; $^{**}P < 0.01$; $^{***}P < 0.001$; $^{****}P < 0.0001$.

activation of the prodrug, as TYMP is required for its conversion to the active antimetabolite 5-FU; and 2) depletion of the nucleoside salvage pathway substrate dT by TYMP and the synergistic depletion of dTTP pools alongside 5-FU–mediated TYMS inhibition (54).

A limitation of this study is the reliance on xenograft tumors in immunodeficient mice, which was necessitated as a consequence of the significant cross-species differences between the nucleotide metabolism of mice and humans. Plasma nucleoside levels are orders of magnitude higher in rodents than in humans, and increasing evidence indicates that this is mechanistically linked to differences in the activity of nucleoside catabolizing enzymes including CDA and adenosine deaminase 2 (22). In particular, we and others have previously reported that dT levels are ∼100 times lower in humans (10 nM) than in mice and rats (1,000 nM) (22, 55, 56). This metabolic species distinction can potentially explain the findings reported in early studies evaluating [^{18}F]FLT, in which tracer bone marrow uptake was noted in dogs and humans (18), in contrast to the low signals observed in mice (15). Furthermore, TYMP is an interferon-regulated gene in human but not in mouse cells (57); thus, modeling the contribution of nontumor cells to STING-driven IFN signaling and [^{18}F]FLT uptake in mice is a significant challenge. Importantly, TYMP has been shown to be induced in peripheral blood mononuclear cells by recombinant IFN therapy in humans (58). While clinical trials are needed to define the utility of our findings, chimeric mouse models engrafted with human fetal liver tissue, fetal thymus tissue, and CD34$^+$ human pluripotent stem cells that possess a "humanized" immune system may provide a platform to evaluate the contribution of immune cells to [^{18}F]FLT PET responses following PRR activation in preclinical settings (59).

In conclusion, we have demonstrated that [^{18}F]FLT PET can visualize metabolic alterations triggered by both genetic and pharmacological STING activation–induced IFN signaling in xenograft tumors. We anticipate that [^{18}F]FLT PET will have utility as a pharmacodynamic readout to guide the translation of STING agonists and potentially other interferon-stimulating therapies.

Methods

Contact for Reagent and Resource Sharing. Reagent or resource requests should be submitted to the lead contact, Caius G. Radu (cradu@mednet.ucla.edu).

Experimental Model and Subject Details.

Cell culture. Cell cultures were maintained as previously described (29). All experiments were performed using cell cultures between passages 3 and 20 maintained in antibiotic-free Dulbecco's modified Eagle's medium (DMEM) +10% fetal bovine serum (FBS) at 37 °C and 5% CO_2. Cell cultures were routinely monitored for mycoplasma contamination using the PCR-based Venor Mycoplasma kit. PDAC cell lines were acquired either from a commercial vendor (American Type Culture Collection or German Collection of Microorganisms and Cell Cultures) or from collaborators. Cell line identity was independently authenticated by PCR (Laragen). Immortalized human pancreatic cancer associated fibroblast cells were provided by Rosa F. Hwang (Department of Surgical Oncology, The University of Texas MD Anderson Cancer Center, Houston, TX).

Drugs. Drug stocks were prepared in dimethylsulfoxide (DMSO) or H_2O and diluted fresh in cell culture media for treatments. The nonhydrolyzable bisphosphorothioate 2′-3′-cGAMP analog and ISD were complexed with Lipofectamine 3000 before treatment.

Animal studies. All animal studies were approved by the University of California, Los Angeles (UCLA) Animal Research Committee. For subcutaneous tumor studies, 6- to 8-wk-old male/female NOD-Prkdc^{em26Cd52}Il2rg^{em26Cd22}/NjuCrl co-isogenic immunodeficient (NCG CRL572; Charles River Laboratories) mice were injected subcutaneously on the flank with 1.0×10^6 cells suspended in phosphate-buffered saline (PBS). Subcutaneous tumor volumes were evaluated by either caliper or CT measurement using a G8 PET/CT scanner (PerkinElmer). For orthotopic tumor studies, SUIT2-TetR-STING^{R284M} cells were engineered to stably express fLUC using lentiviral transduction, and either 5,000 or 30,000 cells were suspended 1:1 in PBS:matrigel (15 μL:15 μL) and injected into the pancreata of NCG mice. A total of 7 d after inoculation, tumor radiance was measured by bioluminesence imaging, and this signal was used to randomize mice to treatment cohorts. For doxycycline (DOX) treatment, mice were supplied with a control or DOX-hyclate supplemented diet intended to deliver a daily dose of 2 to 3 mg of DOX. For STING agonist treatment, mice were administered 100 μL 1.5 mg/kg diABZI compound 3 or vehicle (DMSO + 40% polyethylene glycol 400 in 0.9% saline)

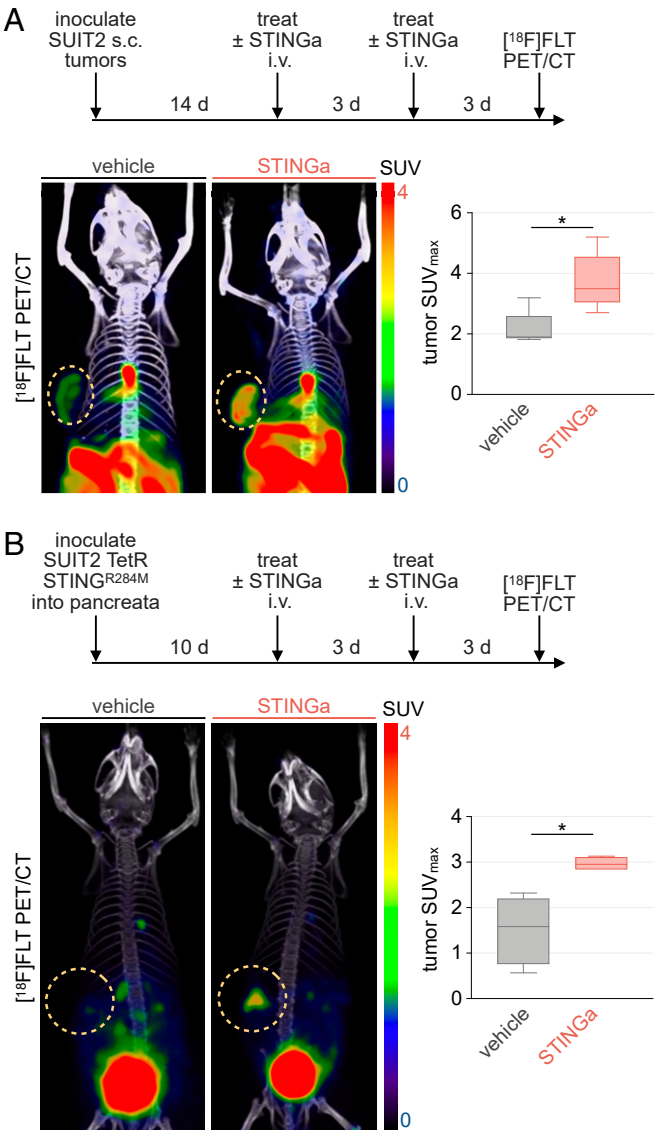

Fig. 5. Systemic STING agonist treatment increases [^{18}F]FLT accumulation in xenograft PDAC tumors. (*A*) [^{18}F]FLT PET/CT imaging of female NCG mice bearing subcutaneous (s.c.) SUIT2 tumors following treatment ± STINGa (1.5 mg/kg; i.v.). Highlighted region indicates tumor (n = 5, two-tailed Mann–Whitney U test). (*B*) [^{18}F]FLT PET/CT imaging of male NCG mice bearing orthotopic SUIT2-TetR-STING^{R284M} tumors following treatment ± STINGa (30,000 cells injected; n = 4, two-tailed Mann–Whitney U test). *$P < 0.05$.

by intravenous tail vein injection. All tumor measurements and calculations were performed by trained technicians blinded to experimental conditions.

Bioluminescence Imaging (BLI). A total of 5 min after intraperitoneal injection of D-luciferin (50 μL at 50 mg/mL in 0.9% saline), mice were anesthetized under 2% isoflurane for 5 additional minutes and imaged using an IVIS Bioluminescence Imaging scanner (PerkinElmer). All images were acquired using a 30-s exposure time and low binning. A region of interest was drawn over whole tumors, and the radiance (p/s) value was recorded. Analysis was performed using Living Image software (PerkinElmer).

PET Imaging. PET/CT imaging studies were conducted as previously described (60). PET and CT images were acquired in sequence using a G8 PET/CT scanner (PerkinElmer) 1.5 h after the administration of 60 μCi [^{18}F]FLT, 1 h after the administration of 20 μCi [^{18}F]FDG, or 1 h after the administration of 35 μCi [^{18}F]FAC by intravenous tail vein injection of prewarmed mice. For [^{18}F]FDG analysis, mice were fasted for 4 h before probe administration, and mice were maintained under anesthesia for the duration of the probe injection, uptake, and imaging periods. PET analysis was performed with either PMOD software (version 3.612, PMOD Technologies Ltd.) or Osirix (Pixmeo). A volume of interest was drawn on whole tumors, and the maximum standard uptake value (SUV_{max}) was recorded. SUV_{max} was used to quantify tumor [^{18}F]FLT, [^{18}F]FDG, or [^{18}F]FAC uptake.

Radiochemical Synthesis of [^{18}F]-labeled Probes. [^{18}F]FLT and [^{18}F]FAC were synthesized using the Elixys Synthesizer (Sofie Biosciences) following published protocols (15, 61). [^{18}F]FDG was obtained from the Biomedical Cyclotron Facility at UCLA.

[^{18}F]-labeled Metabolite Uptake Assay. Radioactive probe uptake assays were conducted as previously described (62). Briefly, cells seeded in 6-well plates were pretreated with IFN-β for 24 h or diABZI for 72 h, respectively, and pulsed with 5 μCi/2 mL of [^{18}F]-labeled probe and dT in DMEM + 10% dialyzed FBS for 2 h. Following incubation, cells were washed three times with 1 mL PBS and lysed using radioimmunoprecipitation assay (RIPA) buffer. Cell lysate radioactivity was measured on a Wizard2 gamma counter (PerkinElmer).

Plasma Collection. Blood was collected in lithium heparin-coated tubes using the retro-orbital technique and stored on ice until plasma isolation. Blood samples were centrifuged at 2,000 × g for 15 min at 4 °C, and plasma supernatants were collected for LC-MS/MS analysis.

Tumor Homogenization. Fragments from resected tumors were weighed (30 to 80 mg), transferred to Omni Hard Tissue homogenization vials, and snap frozen. Either 7.5 μL/mg tissue of lysis buffer (50 mM ammonium bicarbonate, pH 7.2; 0.5% sodium deoxycholate; 12 mM sodium laurel sarcosine supplemented with protease and phosphatase inhibitor mixtures) for immunoblot analysis or 10 μL/mg tissue of metabolite extraction buffer (80% MeOH in water + 0.5 μM ^{13}C,^{15}N-labeled dC and dT) for LC-MS/MS analysis. Samples were homogenized using an Omni Bead Ruptor Elite (eight cycles of 15 s on, 30 s off, speed 8) chilled to 4 °C. Tissue homogenates were cleared by centrifugation at 12,000 × g for 10 min at 4 °C. Cleared lysates were normalized using the bicinchoninic acid (BCA) assay and prepared for immunoblot analysis or analyzed by LC-MS/MS.

Immunoblot Analysis. Immunoblot analysis was performed as previously described (29). PBS-washed cell pellets obtained following trypsinization of cells and centrifugation at 450 × g for 5 min were resuspended in RIPA buffer supplemented with protease and phosphatase inhibitors and incubated at 4 °C for 15 min. Protein concentrations were determined by BCA assay, samples were normalized by RIPA and 4× laemmli loading dye dilution, resolved on 4 to 12% Bis-Tris gels and electrotransferred to a nitrocellulose membrane. After blocking with 5% nonfat milk in tris-buffered saline + 0.1% tween-20 (TBS-T), membranes were incubated overnight in primary antibodies diluted 1:1,000 in 5% BSA in TBS-T. Membranes were subsequently washed with TBS-T and incubated with horseradish peroxidase (HRP)-linked secondary antibodies prepared at a 1:2,500 dilution in 5% nonfat dry milk in TBS-T. HRP was activated by incubating membranes with a mixture of SuperSignal Pico and SuperSignal Femto enhanced chemiluminescence reagents (100:1 ratio). HRP signals were detected by exposure of autoradiography film or imaging using a LI-COR Odyssey system. Antibodies are reported in Key Resource Table (*SI Appendix*).

RT-PCR. Total RNA was isolated from cell cultures using the NucleoSpin RNA kit. Reverse transcription was performed using the High Capacity cDNA Reverse Transcription kit. qPCR was performed using EvaGreen qPCR Master Mix on the QuantStudio3 system. RNA expression values were normalized to housekeeping gene (ACTB) expression, calculated using the $^{\Delta\Delta}$Ct method and displayed as relative expression to control. Primer sequences are reported in Key Resource Table.

Live-Cell Imaging. For live-cell imaging, cells were plated at 2 × 10^3 cells per 100 μL per well in ultra-low attachment (anchorange independent) U-bottom 96-well plates. After 72 h, treatments were added to a final volume of 200 μL and cell proliferation was tracked using the IncuCyte Zoom live-cell imaging system. Images were acquired at 3 h intervals over the indicated time period. Sphere area analysis was applied to quantify proliferation.

Gene Knockdown Using shRNA. For generation of stable knockdown cell lines, PDAC cells were transduced with lentivirus harvested from FT293 cells in the presence of polybrene. For virus production, lentivirval vectors and psPAX2/pMD2G

packaging plasmids at a 2:1:1 ratio were transfected into FT293 cells using polyethylenimine. Lentivirus-containing supernatants were passed through a 0.45-μm filter prior to use. Following transduction, cells underwent antibiotic selection, and knockdown efficiency was confirmed using immunoblot analysis.

Gene KO Using CRISPR/Cas9. All guide RNA (gRNA)-encoding oligonucleotides were cloned into the LentiCrispr version 2 vector. Lipofectamine 3000 was used to transfect PDAC cells with gRNA-specific LentiCrispr version 2 vectors. Following puromycin selection, cells were singly cloned, and gene knockout was confirmed by genomic DNA PCR and tracking of insertions and deletions by decomposition (TIDE) analysis of Sanger sequencing results. Gene knockout was additionally validated using immunoblot analysis.

Generation of DOX-Inducible STING^{R284M} Models. The generation of SUIT2-TetR-STING^{R284M} cells was previously described (19). A STING^{R284M}-encoding gene fragment was ligated into the pENTR-D/TOPO entry vector. Resulting constructs were recombined into pLenti-CMV/TO-GFP/PURO using Gateway LR Clonase II. For virus production, lentivirval vectors and packaging plasmids (psPAX2 and pMD2G) at a 2:1:1 ratio were transfected into FT293 cells using polyethylenimine. Transduced cells were selected in puromycin for 1 wk. In this model, STING^{R284M} expression is regulated by the doxycycline-responsive TetR protein expressed from the pLenti3/EF/GW/IVS-Kozak-TetR-P2A-Bsd vector.

Stable Isotope–labeled Metabolite Tracing, Metabolite Extraction, and DNA Isolation/Hydrolysis. For analysis of stable isotope–labeled metabolite incorporation to media nucleosides or newly replicated DNA, cells were cultured in glucose-free DMEM media supplemented with 10% dialyzed FBS, 4 mM glutamine, and 1 g/L [$^{13}C_6$]glucose ± 1 μM [$^{15}N_2$]dT and treated as indicated. At experimental end points, media was collected and centrifuged at 450 × *g* for 5 min at 4 °C, and the supernatant was stored at −80 °C before analysis. Genomic DNA was extracted as previously described using the Zymo Quick-genomic DNA MiniPrep kit and hydrolyzed to nucleosides using the DNA Degradase Plus kit, following manufacturer-supplied instructions (29). A total of 50 μL water was used to elute DNA into a 1.5-mL microcentrifuge tube. A nuclease solution (5 μL; 10× buffer/DNA Degradase Plus/water, 2.5/1/1.5, vol/vol/v) was added to 20 μL eluted genomic DNA in an high performance liquid chromatography injector vial. Samples were incubated overnight at 37 °C before analysis. For media and plasma metabolite extraction, 20 μL of the sample was mixed with 80 μL 100% MeOH containing stable isotope–labeled nucleoside internal standards (0.5 μM ^{13}C, ^{15}N-labeled dC, and dT). MeOH-extracted samples were incubated at −80 °C for 24 h before analysis.

Mass Spectrometry. Analysis of hydrolyzed DNA, media, serum, and tumor nucleoside levels was performed as previously described (27). An aliquot of MeOH-extracted samples or hydrolyzed DNA (5 μL) was injected onto a porous graphitic carbon column (Thermo Fisher Scientific Hypercarb, 100 × 2.1 mm, 5-μm particle size) equilibrated in solvent A (water 0.1% formic acid, vol/vol) and eluted (200 μL/min) with an increasing concentration of solvent B (acetonitrile 0.1% formic acid, vol/vol) using min/%B/flow rates (μL/min) as follows: 0/0/200, 5/0/200, 10/15/200, 20/15/200, 21/40/200, 25/50/200, 26/100/700, 30/100/700, 31/0/700, 34/0/700, and 35/0/200. The effluent from the column was directed to the Agilent Jet Stream ion source connected to a triple quadrupole mass spectrometer (Agilent 6460) operating in the MRM mode using previously optimized settings. The peak areas for each nucleoside (precursor → fragment ion transitions) at predetermined retention times were recorded using the software supplied by the instrument manufacturer (Agilent MassHunter). Peak areas were normalized to nucleoside internal standard signals. An external standard curve was applied to determine plasma and media nucleoside concentrations.

RNA-seq. SUIT2 cells were seeded overnight in 6-well plates and treated ± 100 U/mL IFN-β for 24 h. Following treatment, messenger RNA (mRNA) was extracted as described for RT-PCR analysis and processed for next-generation sequencing. The analysis workflow consisted of mRNA capture, complementary DNA generation, end repair to generate blunt ends, A-tailing, adaptor ligation, and PCR amplification. Libraries were sequenced on Illumina HiSeq 3000 on a single-read 50-bp run. An FDR of <0.01% was applied to filter significantly altered transcripts.

Statistical Analyses. Statistical analysis was performed as previously described (29). Data are presented as mean ± SD with the number of biological replicates indicated. Comparisons of two groups were calculated using the indicated unpaired two-tailed Student's *t* test, and *P* values less than 0.05 were considered significant. Comparisons of more than two groups were calculated using one-way ANOVA followed by Bonferroni's multiple comparison tests, and *P* values less than 0.05/m, where m is the total number of possible comparisons, were considered significant. The two-tailed Mann–Whitney *U* test was applied for two-group comparisons of tumor SUV values obtained by PET imaging.

Data Availability. RNA-seq data have been deposited in the National Center for Biotechnology Information Gene Expression Omnibus (GEO: GSE178901). The RNA-seq dataset described in Fig. 1*A* is included as Dataset S1. All other study data are included in the article and/or supporting information.

ACKNOWLEDGMENTS. We thank Joel Almajano, Firas Hikmat, and Kyle Current for assistance with performing the animal studies. We thank all members of the Ahmanson Translational Imaging Division at UCLA for their advice, technical expertise, and support. This work was supported by an NIH R01 Grant 1R01CA250529-01A1. E.R.A. is supported by UCLA Tumor Immunology Training Grant T32CA009120.

1. B. S. Parker, J. Rautela, P. J. Hertzog, Antitumour actions of interferons: Implications for cancer therapy. *Nat. Rev. Cancer* **16**, 131–144 (2016).
2. L. M. Snell, T. L. McGaha, D. G. Brooks, Type I interferon in chronic virus infection and cancer. *Trends Immunol.* **38**, 542–557 (2017).
3. D. A. Hoagland *et al*., Leveraging the antiviral type I interferon system as a first line of defense against SARS-CoV-2 pathogenicity. *Immunity* **54**, 557–570.e5 (2021).
4. H. Tanji *et al*., Toll-like receptor 8 senses degradation products of single-stranded RNA. *Nat. Struct. Mol. Biol.* **22**, 109–115 (2015).
5. M. Motwani, S. Pesiridis, K. A. Fitzgerald, DNA sensing by the cGAS-STING pathway in health and disease. *Nat. Rev. Genet.* **20**, 657–674 (2019).
6. C. Vanpouille-Box, S. Demaria, S. C. Formenti, L. Galluzzi, Cytosolic DNA sensing in organismal tumor control. *Cancer Cell* **34**, 361–378 (2018).
7. J. M. Ramanjulu *et al*., Design of amidobenzimidazole STING receptor agonists with systemic activity. *Nature* **564**, 439–443 (2018).
8. J. Kwon, S. F. Bakhoum, The cytosolic DNA-sensing cGAS-STING pathway in cancer. *Cancer Discov.* **10**, 26–39 (2020).
9. G. Berger, M. Marloye, S. E. Lawler, Pharmacological modulation of the STING pathway for cancer immunotherapy. *Trends Mol. Med.* **25**, 412–427 (2019).
10. B. S. Pan *et al*., An orally available non-nucleotide STING agonist with antitumor activity. *Science* **369**, eaba6098 (2020).
11. E. N. Chin *et al*., Antitumor activity of a systemic STING-activating non-nucleotide cGAMP mimetic. *Science* **369**, 993–999 (2020).
12. J. R. Baird *et al*., Radiotherapy combined with novel STING-targeting oligonucleotides results in regression of established tumors. *Cancer Res.* **76**, 50–61 (2016).
13. Vonderhaar EP *et al*. STING activated tumor-intrinsic type I interferon signaling promotes CXCR3 dependent antitumor immunity in pancreatic cancer. *Cell Mol. Gastroenterol. Hepatol.* **12**, 41–58 (2021).
14. H. Cheon *et al*., IFNβ-dependent increases in STAT1, STAT2, and IRF9 mediate resistance to viruses and DNA damage. *EMBO J.* **32**, 2751–2763 (2013).
15. C. G. Radu *et al*., Molecular imaging of lymphoid organs and immune activation by positron emission tomography with a new [18F]-labeled 2′-deoxycytidine analog. *Nat. Med.* **14**, 783–788 (2008).
16. C. Beinat *et al*., The characterization of ^{18}F-hGTS13 for molecular imaging of x_C^- transporter activity with PET. *J. Nucl. Med.* **60**, 1812–1817 (2019).
17. J. T. Lee, D. O. Campbell, N. Satyamurthy, J. Czernin, C. G. Radu, Stratification of nucleoside analog chemotherapy using 1-(2′-deoxy-2′-18F-fluoro-β-D-arabinofuranosyl)cytosine and 1-(2′-deoxy-2′-18F-fluoro-β-L-arabinofuranosyl)-5-methylcytosine PET. *J. Nucl. Med.* **53**, 275–280 (2012).
18. A. F. Shields *et al*., Imaging proliferation in vivo with [F-18]FLT and positron emission tomography. *Nat. Med.* **4**, 1334–1336 (1998).
19. A. M. Moore *et al*., NAD^+ depletion by type I interferon signaling sensitizes pancreatic cancer cells to NAMPT inhibition. *Proc. Natl. Acad. Sci. U.S.A.* **118**, e2012469118 (2021).
20. X. Lang *et al*., Radiotherapy and mmunotherapy promote tumoral lipid oxidation and ferroptosis via synergistic repression of SLC7A11. *Cancer Discov.* **9**, 1673–1685 (2019).
21. C. C. Zhang *et al*., [(18)F]FLT-PET imaging does not always "light up" proliferating tumor cells. *Clin. Cancer Res.* **18**, 1303–1312 (2012).
22. W. Kim *et al*., [18F]CFA as a clinically translatable probe for PET imaging of deoxycytidine kinase activity. *Proc. Natl. Acad. Sci. U.S.A.* **113**, 4027–4032 (2016).
23. D. C. Goldstone *et al*., HIV-1 restriction factor SAMHD1 is a deoxynucleoside triphosphate triphosphohydrolase. *Nature* **480**, 379–382 (2011).
24. J. Nomme *et al*., Structure-guided development of deoxycytidine kinase inhibitors with nanomolar affinity and improved metabolic stability. *J. Med. Chem.* **57**, 9480–9494 (2014).
25. T. M. Le *et al*., ATR inhibition facilitates targeting of leukemia dependence on convergent nucleotide biosynthetic pathways. *Nat. Commun.* **8**, 241 (2017).
26. S. J. Lee *et al*., Thymidine phosphorylase influences [(18)F]fluorothymidine uptake in cancer cells and patients with non-small cell lung cancer. *Eur. J. Nucl. Med. Mol. Imaging* **41**, 1327–1335 (2014).

27. D. A. Nathanson *et al*., Co-targeting of convergent nucleotide biosynthetic pathways for leukemia eradication. *J. Exp. Med.* **211**, 473–486 (2014).
28. A. Bronckaers, F. Gago, J. Balzarini, S. Liekens, The dual role of thymidine phosphorylase in cancer development and chemotherapy. *Med. Res. Rev.* **29**, 903–953 (2009).
29. E. R. Abt *et al*., Metabolic modifier screen reveals secondary targets of protein kinase inhibitors within nucleotide metabolism. *Cell Chem. Biol.* **27**, 197–205.e6 (2020).
30. V. Guarcello, C. Blanquicett, F. N. Naguib, M. H. El Kouni, Suppression of thymidine phosphorylase expression by promoter methylation in human cancer cells lacking enzyme activity. *Cancer Chemother. Pharmacol.* **62**, 85–96 (2008).
31. M. Ghandi *et al*., Next-generation characterization of the cancer cell line encyclopedia. *Nature* **569**, 503–508 (2019).
32. C. Feig *et al*., The pancreas cancer microenvironment. *Clin. Cancer Res.* **18**, 4266–4276 (2012).
33. D. L. Burdette *et al*., STING is a direct innate immune sensor of cyclic di-GMP. *Nature* **478**, 515–518 (2011).
34. E. D. Tang, C. Y. Wang, Single amino acid change in STING leads to constitutive active signaling. *PLoS One* **10**, e0120090 (2015).
35. A. F. Shields, PET imaging of tumor growth: Not as easy as it looks. *Clin. Cancer Res.* **18**, 1189–1191 (2012).
36. V. K. Gonugunta *et al*., Trafficking-mediated STING degradation requires sorting to acidified endolysosomes and can be targeted to enhance anti-tumor response. *Cell Rep.* **21**, 3234–3242 (2017).
37. E. Nistal-Villan *et al*., A versatile vector for in vivo monitoring of type I interferon induction and signaling. *PLoS One* **11**, e0152031 (2016).
38. J. L. Sherley, T. J. Kelly, Regulation of human thymidine kinase during the cell cycle. *J. Biol. Chem.* **263**, 8350–8358 (1988).
39. A. F. Shields, K. Lim, J. Grierson, J. Link, K. A. Krohn, Utilization of labeled thymidine in DNA synthesis: Studies for PET. *J. Nucl. Med.* **31**, 337–342 (1990).
40. V. R. Bollineni, G. M. Kramer, E. P. Jansma, Y. Liu, W. J. Oyen, A systematic review on [(18)F]FLT-PET uptake as a measure of treatment response in cancer patients. *Eur. J. Cancer* **55**, 81–97 (2016).
41. W. Chen *et al*., Imaging proliferation in brain tumors with 18F-FLT PET: Comparison with 18F-FDG. *J. Nucl. Med.* **46**, 945–952 (2005).
42. B. S. Pio *et al*., Usefulness of 3′-[F-18]fluoro-3′-deoxythymidine with positron emission tomography in predicting breast cancer response to therapy. *Mol. Imaging Biol.* **8**, 36–42 (2006).
43. B. E. Ueberroth *et al*., The use of 3′-deoxy-3′-^{18}F-fluorothymidine (FLT) PET in the assessment of long-term survival in breast cancer patients treated with neoadjuvant chemotherapy. *Ann. Nucl. Med.* **33**, 383–393 (2019).
44. H. Barthel *et al*., 3′-deoxy-3′-[18F]fluorothymidine as a new marker for monitoring tumor response to antiproliferative therapy in vivo with positron emission tomography. *Cancer Res.* **63**, 3791–3798 (2003).
45. V. Frings *et al*., Pemetrexed induced thymidylate synthase inhibition in non-small cell lung cancer patients: A pilot study with 3′-deoxy-3′-[^{18}F]fluorothymidine positron emission tomography. *PLoS One* **8**, e63705 (2013).
46. H. J. Lee *et al*., Positron emission tomography imaging of human colon cancer xenografts in mice with [18F]fluorothymidine after TAS-102 treatment. *Cancer Chemother. Pharmacol.* **75**, 1005–1013 (2015).
47. P. Wells *et al*., 2-[11C]thymidine positron emission tomography as an indicator of thymidylate synthase inhibition in patients treated with AG337. *J. Natl. Cancer Inst.* **95**, 675–682 (2003).
48. D. A. Plotnik, L. J. McLaughlin, J. Chan, J. N. Redmayne-Titley, J. L. Schwartz, The role of nucleoside/nucleotide transport and metabolism in the uptake and retention of 3′-fluoro-3′-deoxythymidine in human B-lymphoblast cells. *Nucl. Med. Biol.* **38**, 979–986 (2011).
49. A. Ribas *et al*., Imaging of CTLA4 blockade-induced cell replication with (18)F-FLT PET in patients with advanced melanoma treated with tremelimumab. *J. Nucl. Med.* **51**, 340–346 (2010).
50. E. H. Aarntzen *et al*., Early identification of antigen-specific immune responses in vivo by [18F]-labeled 3′-fluoro-3′-deoxy-thymidine ([18F]FLT) PET imaging. *Proc. Natl. Acad. Sci. U.S.A.* **108**, 18396–18399 (2011).
51. D. Wu *et al*., Type 1 interferons induce changes in core metabolism that are critical for immune function. *Immunity* **44**, 1325–1336 (2016).
52. A. G. York *et al*., Limiting cholesterol biosynthetic flux spontaneously engages type I IFN signaling. *Cell* **163**, 1716–1729 (2015).
53. E. Marangoni *et al*., Capecitabine efficacy is correlated with TYMP and RB1 expression in PDX established from triple-negative breast cancers. *Clin. Cancer Res.* **24**, 2605–2615 (2018).
54. E. A. Choi *et al*., Combined 5-fluorouracil/systemic interferon-beta gene therapy results in long-term survival in mice with established colorectal liver metastases. *Clin. Cancer Res.* **10**, 1535–1544 (2004).
55. K. M. Li, L. P. Rivory, S. J. Clarke, Rapid quantitation of plasma 2′-deoxyuridine by high-performance liquid chromatography/atmospheric pressure chemical ionization mass spectrometry and its application to pharmacodynamic studies in cancer patients. *J. Chromatogr. B Analyt. Technol. Biomed. Life Sci.* **820**, 121–130 (2005).
56. H. Nottebrock, R. Then, Thymidine concentrations in serum and urine of different animal species and man. *Biochem. Pharmacol.* **26**, 2175–2179 (1977).
57. I. Rusinova *et al*., Interferome v2.0: An updated database of annotated interferon-regulated genes. *Nucleic Acids Res.* **41**, D1040–D1046 (2013).
58. D. Makower, S. Wadler, H. Haynes, E. L. Schwartz, Interferon induces thymidine phosphorylase/platelet-derived endothelial cell growth factor expression in vivo. *Clin. Cancer Res.* **3**, 923–929 (1997).
59. M. A. Carrillo, A. Zhen, S. G. Kitchen, The use of the humanized mouse model in gene therapy and immunotherapy for HIV and cancer. *Front. Immunol.* **9**, 746 (2018).
60. C. J. Shu *et al*., Novel PET probes specific for deoxycytidine kinase. *J. Nucl. Med.* **51**, 1092–1098 (2010).
61. J. Collins *et al*., Production of diverse PET probes with limited resources: 24 ^{18}F-labeled compounds prepared with a single radiosynthesizer. *Proc. Natl. Acad. Sci. U.S.A.* **114**, 11309–11314 (2017).
62. D. O. Campbell *et al*., Structure-guided engineering of human thymidine kinase 2 as a positron emission tomography reporter gene for enhanced phosphorylation of non-natural thymidine analog reporter probe. *J. Biol. Chem.* **287**, 446–454 (2012).